Novel methods to measure the gravitational constant in space

M. Armano,[1] H. Audley,[2] J. Baird,[3,†] P. Binetruy,[3,*] M. Born,[2] D. Bortoluzzi,[4] E. Castelli,[5] A. Cavalleri,[6] A. Cesarini,[7] A. M. Cruise,[8] K. Danzmann,[2] M. de Deus Silva,[9] I. Diepholz,[2] G. Dixon,[8] R. Dolesi,[5] L. Ferraioli,[10] V. Ferroni,[5] E. D. Fitzsimons,[11] M. Freschi,[9] L. Gesa,[12,13] F. Gibert,[5,14] D. Giardini,[10] R. Giusteri,[2] C. Grimani,[7] J. Grzymisch,[1] I. Harrison,[15] M-S Hartig,[2] G. Heinzel,[2] M. Hewitson,[2] D. Hollington,[16] D. Hoyland,[8] M. Hueller,[5] H. Inchauspé,[3,17] O. Jennrich,[1] P. Jetzer,[18] N. Karnesis,[3] B. Kaune,[2] N. Korsakova,[19] C. J. Killow,[19] J. A. Lobo,[12,13,*] L. Liu,[5] J. P. López-Zaragoza,[12] R. Maarschalkerweerd,[15] D. Mance,[10] N. Meshksar,[10] V. Martín,[12,13] L. Martin-Polo,[9] J. Martino,[3] F. Martin-Porqueras,[9] P. W. McNamara,[1] J. Mendes,[15] L. Mendes,[9] M. Nofrarias,[12,13] S. Paczkowski,[2] M. Perreur-Lloyd,[19] A. Petiteau,[3] P. Pivato,[5] E. Plagnol,[3] J. Ramos-Castro,[20,13] J. Reiche,[2] D. I. Robertson,[19] F. Rivas,[12,13] G. Russano,[5] J. Slutsky,[21] C. F. Sopuerta,[12,13] T. Sumner,[16] D. Texier,[9] J. I. Thorpe,[21] C. Trenkel,[22] D. Vetrugno,[5] S. Vitale,[5] G. Wanner,[2] H. Ward,[19] P. J. Wass,[16,17] W. J. Weber,[5] L. Wissel,[2] A. Wittchen,[2] and P. Zweifel[10]

(LISA Pathfinder Collaboration)

[1]*European Space Technology Centre, European Space Agency, Keplerlaan 1, 2200 AG Noordwijk, Netherlands*
[2]*Albert-Einstein-Institut, Max-Planck-Institut für Gravitationsphysik und Leibniz Universität Hannover, Callinstraße 38, 30167 Hannover, Germany*
[3]*APC, Univ Paris Diderot, CNRS/IN2P3, CEA/lrfu, Obs de Paris, Sorbonne Paris Cité, France*
[4]*Department of Industrial Engineering, University of Trento, via Sommarive 9, 38123 Trento, and Trento Institute for Fundamental Physics and Application/INFN*
[5]*Dipartimento di Fisica, Università di Trento and Trento Institute for Fundamental Physics and Application/INFN, 38123 Povo, Trento, Italy*
[6]*Istituto di Fotonica e Nanotecnologie, CNR-Fondazione Bruno Kessler, I-38123 Povo, Trento, Italy*
[7]*DISPEA, Università di Urbino "Carlo Bo," Via Santa Chiara, 27 61029 Urbino/INFN, Italy*
[8]*The School of Physics and Astronomy, University of Birmingham, Birmingham, United Kingdom*
[9]*European Space Astronomy Centre, European Space Agency, Villanueva de la Cañada, 28692 Madrid, Spain*
[10]*Institut für Geophysik, ETH Zürich, Sonneggstrasse 5, CH-8092, Zürich, Switzerland*
[11]*The UK Astronomy Technology Centre, Royal Observatory, Edinburgh, Blackford Hill, Edinburgh, EH9 3HJ, United Kingdom*
[12]*Institut de Ciències de l'Espai (ICE, CSIC), Campus UAB, Carrer de Can Magrans s/n, 08193 Cerdanyola del Vallès, Spain*
[13]*Institut d'Estudis Espacials de Catalunya (IEEC), C/ Gran Capità 2-4, 08034 Barcelona, Spain*
[14]*isardSAT SL, Marie Curie 8-14, 08042 Barcelona, Catalonia, Spain*
[15]*European Space Operations Centre, European Space Agency, 64293 Darmstadt, Germany*
[16]*High Energy Physics Group, Physics Department, Imperial College London, Blackett Laboratory, Prince Consort Road, London, SW7 2BW, United Kingdom*
[17]*Department of Mechanical and Aerospace Engineering, MAE-A, P.O. Box 116250, University of Florida, Gainesville, Florida 32611, USA*
[18]*Physik Institut, Universität Zürich, Winterthurerstrasse 190, CH-8057 Zürich, Switzerland*
[19]*SUPA, Institute for Gravitational Research, School of Physics and Astronomy, University of Glasgow, Glasgow, G12 8QQ, United Kingdom*
[20]*Department d'Enginyeria Electrònica, Universitat Politècnica de Catalunya, 08034 Barcelona, Spain*
[21]*Gravitational Astrophysics Lab, NASA Goddard Space Flight Center, 8800 Greenbelt Road, Greenbelt, Maryland 20771, USA*
[22]*Airbus Defence and Space, Gunnels Wood Road, Stevenage, SG1 2AS, United Kingdom*

(Received 25 July 2019; published 20 September 2019)

[*]Deceased.
[†]Corresponding author.
baird@apc.in2p3.fr

We present two novel methods, tested by LISA Pathfinder, to measure the gravitational constant G for the first time in space. Experiment 1 uses electrostatic suspension forces to measure a change in acceleration of a test mass due to a displaced source mass. Experiment 2 measures a change in relative acceleration between two test masses due to a slowly varying fuel tank mass. Experiment 1 gave a value of $G = 6.71 \pm 0.42(\times 10^{-11})$ $m^3\,s^{-2}\,kg^{-1}$ and experiment 2 gave $6.15 \pm 0.35(\times 10^{-11})$ $m^3\,s^{-2}\,kg^{-1}$, both consistent with each other to 1σ and with the CODATA 2014 recommended value of $6.67408 \pm 0.00031(\times 10^{-11})$ $m^3\,s^{-2}\,kg^{-1}$ to 2σ. We outline several ideas to improve the results for a future experiment, and we suggest that a measurement in space would isolate many terrestrial issues that could be responsible for the inconsistencies between recent measurements.

DOI: 10.1103/PhysRevD.100.062003

I. INTRODUCTION

The gravitational constant G has proven to be one of the most difficult constants of nature to measure. Results over the years have shown that although individual experiments have reached relative uncertainties of parts in 10^5 [1–6], the disagreement between them remains at just below parts in 10^3 [7]. It is therefore becoming more important to develop new methods of measuring this constant to shed light on the disagreement.

Since the source of the scatter is thought to be due to errors not accounted for [8,9], it follows that a measurement in space, as a new experimental method in a novel environment, would be informative in future global averages (such as the CODATA values). If precise enough, it could provide a compelling and unbiased complementary measurement independent of many sources of error that could explain the observed scatter, e.g., unbalanced local gravitational fields.

The aim of this work is to discuss two possible methods for a space based interferometry measurement, with an emphasis on which method would be easiest to improve for the future. It is hoped that these analyses will highlight first steps to reach a relative uncertainty competitive with terrestrial measurements.

LISA Pathfinder (LPF) [10] was a drag-free interferometer located at the first Lagrange point in space between the Earth and Sun. It measured the differential acceleration between two gold-platinum test masses suspended in drag-free control. By the end of its lifetime, it had surpassed both its requirements and those of its full scale model LISA [11]. Given the success of the mission, and in coordination with other system tests, a handful of days near the end of the mission extension were allocated to performing a dedicated big G experiment for the first time in space. However, because Pathfinder was not designed to perform this sort of measurement, it was known that systematics such as absolute distances would limit the results to no better than 1% relative uncertainty.

Section II of this work reports the results of a dedicated experiment, which varied the distance between two test masses to source a signal. Section III describes a second method that varied a mass in time to provide a signal. The first experiment is used as a benchmark for experiments not in drag-free control, while the second illustrates the relative ease and cleanliness of a method in drag-free control.

II. EXPERIMENT 1

A. Method

The principle of this experiment is to measure a change in force on a test mass due to a displacement of a source mass. In LPF, this was achieved using the electrostatic forces that suspended the two test masses. A controlled displacement of one test mass would induce a change in the electrostatic restoring control force on the second test mass that is proportional to G.

More precisely, one of the gold-platinum masses, labeled the source mass (SM), is moved a large distance[1] of 600, 900 or 1200 μm away from the second mass, labeled the test mass (TM). A 20 min dwell time is allowed for the control system to settle. The source mass is then moved a large distance in the opposite direction, and left to dwell again. The difference in the suspension forces required to hold the test mass stationary is then proportional to the change in gravitational force on the test mass due to the change in proximity of the source mass, as illustrated in Fig. 1(a), taken from the experiment design document [12].

Since the signal is measured using the electrostatic suspension forces in the SM-TM direction, LPF's state of the art drag-free control cannot be used as it requires no forces applied to the TM in this direction. As a result, the thrusters must be switched off through each measurement to avoid drowning the signal in noise. This then leaves the spacecraft motion uncorrected for the influence of the solar radiation pressure (SRP) flux from the sun, causing it to "sail" both translationally and rotationally due to the geometry of the solar array and a small offset of the spacecraft center of mass. The dominant effect on the TM was a small component of the SRP force leaking into the

[1]Large relative to the distance between test mass faces and electrode housing (4 mm), and relative to distances used in the LPF nominal mission ($\lesssim 1$ μm).

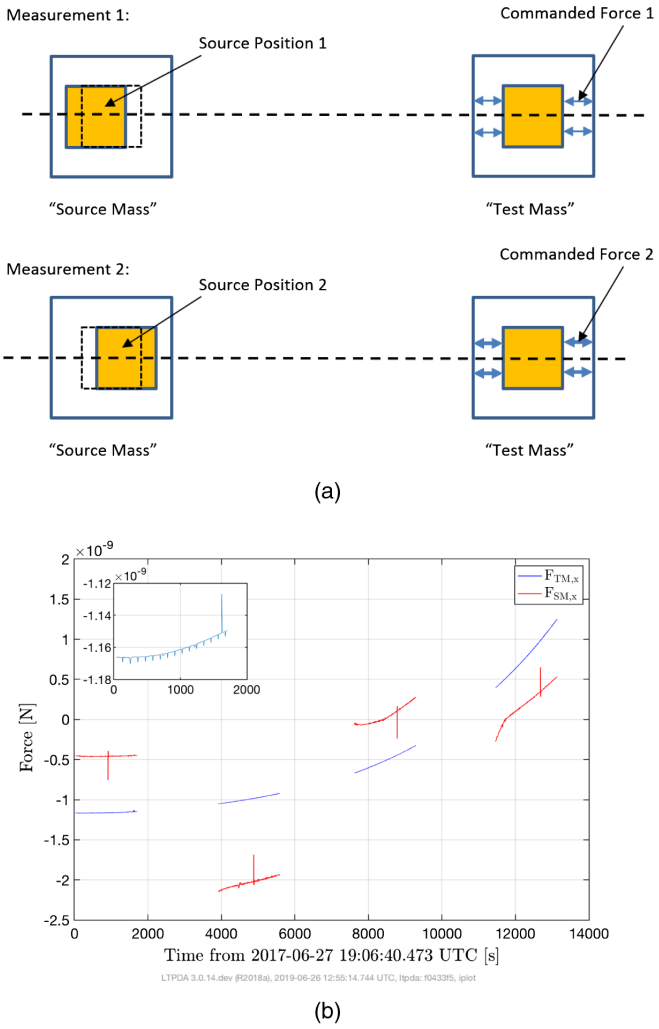

FIG. 1. (a) In the experimental procedure [12], a source mass is moved from positive to negative displacement, and the change in force to hold the test mass stationary is then proportional to the change in gravitational force on the TM. (b) Suspension forces on TM and SM through a signal run are shown. Note the four step changes in the SM force that cause the large displacement within the housing, and a general trend in the data indicating background sources of noise to be characterized and subtracted. Inset: The first high resolution section of $F_{\mathrm{TM},x}$ data, where periodic glitches can be seen. Larger glitches are also observed in almost every $F_{\mathrm{SM},x}$ dwell time, and are likely related to the periodic glitches in $F_{\mathrm{TM},x}$.

measurement axis as the spacecraft rotated during each sail. The rotational velocity of the spacecraft also induced a centrifugal force $F_{\mathrm{Cent},x}$ on the masses, although not as large as the SRP leakage.

Figure 1(b) shows the suspension forces acting on both the TM and SM for a typical signal run in this experiment. Clearly seen is a steady and accelerating background drift. This is a combination of centrifugal and SRP forces acting on the spacecraft and leaking into the measured forces on both masses. Also noted are the step changes in the forces on the masses as the control system works to displace the SM in its housing.

The rotational motion of the spacecraft also limited the time allowed per solar sail to avoid it rotating beyond its allowed limits, and consequently only allowing four source mass dwell times per solar sail. This afforded two independent differences between positive and negative SM displacement dwell times, and therefore two independent fits for G per solar sail. The sail was repeated 10 times, with the final solar sail half as long, giving a total of 19 independent fits for G. An additional 4 h long blank run, where a solar sail was executed with no source mass displacement, was used to assess the magnitude of the SRP force component in the measurement axis, $F_{\mathrm{Rad},x}$. Furthermore, an injected sinusoidal force was also used to fit for the gain g_{TM} between a requested electrostatic force on the TM in the x direction, $F_{\mathrm{TM},x}$, and the actual force applied.

Using superscripts to indicate the source mass position, and labeling the test mass position relative to the spacecraft as measured by the interferometry system, o_{TM}, the residual change in acceleration of the test mass between the positive and negative source mass dwell times, after accounting for all of the known forces during a solar sail, can be written as

$$\begin{aligned} a^{(2)}_{\mathrm{Grav,SM}} - a^{(1)}_{\mathrm{Grav,SM}} = &-(\ddot{o}^{(2)}_{\mathrm{TM}} - \ddot{o}^{(1)}_{\mathrm{TM}}) + \frac{g_{\mathrm{TM}}}{m_{\mathrm{TM}}}(F^{(2)}_{\mathrm{TM},x} - F^{(1)}_{\mathrm{TM},x}) \\ &+ \frac{1}{m_{\mathrm{TM}}}(F^{(2)}_{\mathrm{Rad},x} - F^{(1)}_{\mathrm{Rad},x}) \\ &+ \frac{1}{m_{\mathrm{TM}}}(F^{(2)}_{\mathrm{Cent},x} - F^{(1)}_{\mathrm{Cent},x}) \end{aligned} \tag{1}$$

where m_{TM} is the mass of the test mass, and $a_{\mathrm{Grav,SM}}$ is the acceleration of the test mass due to the source mass. Note that because the test mass is stationary relative to its housing, the contribution from the surrounding spacecraft material cancels in the difference between the positive and negative SM displacements.

Equation (1) shows the leading order contributions to the measured change in force on the TM. When considering the next order corrections, it would be necessary to include a time derivative of the TM suspension force and a delay parameter to account for delays in the control loops. It would also be necessary to include the backreaction on the spacecraft from forces applied on the SM. However, as can be seen in the large forces acting between dwell times to move the SM in Fig. 1(b), the peaks in $F_{\mathrm{SM},x}$ are significantly lower and give an estimated contribution of below 1% to the measured signal. These terms are therefore neglected in this analysis given the best case scenario is a measurement around several percent. For this reason the larger glitches observed in $F_{\mathrm{SM},x}$ will not be discussed later in the same detail as the periodic glitches observed in $F_{\mathrm{TM},x}$, although the two are likely related.

This analysis is split into three stages. The first is a frequency space Monte Carlo fit for the gain using an injected force calibration tone, followed by a linear least squares fit for the SRP force using the blank run, and finally

a second linear least squares fit for the gravitational constant using the remaining signal runs. The details and results of each fit will be presented separately in the following sections.

B. Electrostatic force gain

To fit for the gain, g_{TM}, a force calibration tone was injected in $F_{\mathrm{TM},x}$ at 10 and 30 mHz during a solar sail. The response of the test mass motion, as measured by the interferometer relative to the spacecraft, is used with the force requested to fit for a gain in frequency space. The power spectral density (PSD) of the residual injection acceleration, $\tilde{a}^{\mathrm{inj}}_{\mathrm{TM}}$, is simplified to only two terms given by

$$\tilde{a}^{\mathrm{inj}}_{\mathrm{TM}} = \tilde{\ddot{o}}^{\mathrm{inj}}_{\mathrm{TM}} - \frac{g_{\mathrm{TM}}}{m_{\mathrm{TM}}} \tilde{F}^{\mathrm{inj}}_{\mathrm{TM},x} \tag{2}$$

where tilde represents a PSD, when fitting in the range $[8 \times 10^{-3}\ \mathrm{Hz}, 3.8 \times 10^{-2}\ \mathrm{Hz}]$. This simplification occurs as the spacecraft rotation, and therefore the SRP, centrifugal and gravitational terms, evolves at much lower frequencies outside of the fitting range. The residual acceleration is compared to the same expression computed for the blank run, where a solar sail was performed with no injection. By minimizing the difference between the injection residual and blank run residuals in the fitting range, the algorithm can find the best fit gain and an error using the mean and standard deviation of the posterior distribution.

Figure 2 (bottom panel) shows the time series of the injected force in the x direction on the TM (red) and the response in the second time derivative of the TM position relative to the spacecraft (blue). Looking at the out of loop force $\ddot{o}_{\mathrm{TM}} - F_{\mathrm{TM},x}/m_{\mathrm{TM}}$ (black), which has been detrended to remove the slow drift of the SRP term for better visualization, periodic glitches in the data are seen around 10^{-2} Hz. These were observed in $F_{\mathrm{TM},x}$ [e.g., Fig. 1(b), where larger amplitude glitches are also observed in $F_{\mathrm{SM},x}$ that are likely related in origin] and o_{TM} for all SM dwell times, and they are thought to come from clock synchronization errors when the spacecraft was in configurations that applied variable suspension forces to both test masses. Although the periodicity of the $F_{\mathrm{TM},x}$ glitches is regular, the shape is not, making their subtraction very difficult. Furthermore, their 100s periodicity is exactly at the calibration tone frequency, making their influence on the fits non-negligible.

Figure 2 (top panel) shows the amplitude spectral densities (ASD) of the injection tone residuals (red) and the blank run evaluation of the model (yellow), with the original calibration tone ASD for comparison (blue). Note the two residuals still exhibit a periodic structure at the frequency of the glitches and harmonics thereof. This suggests that the calibration tone was loud enough to fit for the gain, but the posterior error is larger than in nominal

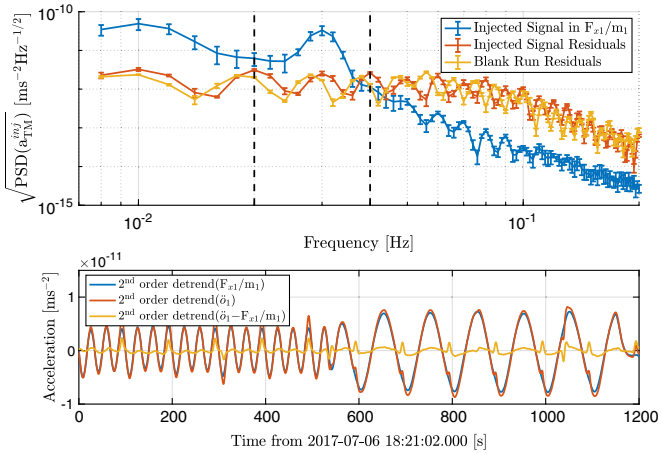

FIG. 2. Top: Amplitude spectral densities of the injected TM acceleration (blue) and the residuals of the best fit model evaluated for the injection data (red) and the blank run (yellow). Dashed black vertical lines indicate the fitting range used in the algorithm. Bottom: By taking the injected acceleration (blue) and subtracting the TM movement as measured by the interferometer (red) the out of loop acceleration (yellow) shows the presence of periodic glitches roughly every 100s. These coincide with the lower frequency injection, making the fits for the gain not as sensitive as in previous experiments.

mission fits for the same parameter, as the blank run also exhibited glitches.

Figure 3 shows the posterior distribution for the gain, with central value and 1σ error 1.0786 ± 0.0095. This is in close agreement with the system identification experiments, where the gain on the equivalent test mass was measured at 1.0748 ± 0.0001 [13]. A good agreement in posterior value is observed as expected, indicating the goodness of the fit, with a larger relative error substantiating the impact of the glitches on the posterior.

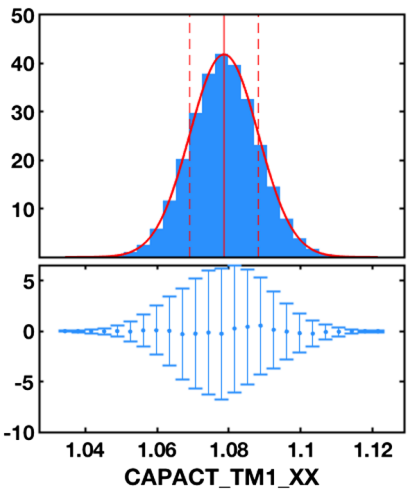

FIG. 3. Top: Posterior distribution of TM electrostatic gain. Bottom: Residual errors after fitting a Gaussian to the posterior.

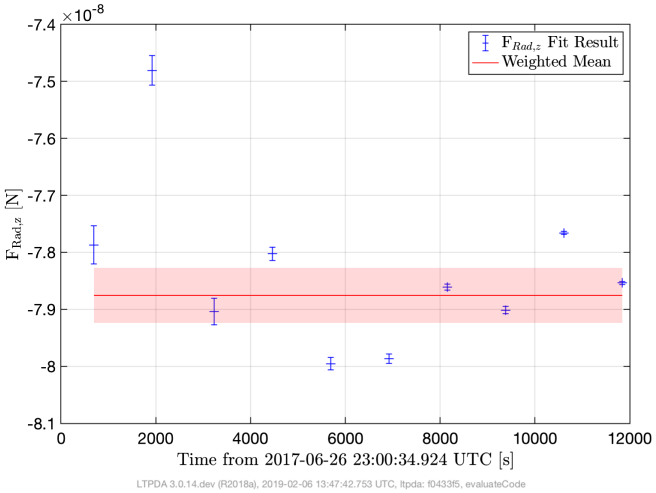

FIG. 4. Fit results for $F_{\mathrm{Rad},Z}$, using 20 segments of the blank run for 10 independent fits.

C. Solar radiation pressure

As the spacecraft rotated through a solar sail, a component of the relatively large SRP force on the spacecraft entered into the TM-SM axis. Assuming a constant SRP force in the Sun-Earth direction, $F_{\mathrm{Rad},Z'}$, it is possible to subtract this component from the electrostatic force on the SM using the projection

$$F_{\mathrm{Rad},x} = (\cos(\theta_{\mathrm{SC}})\sin(\eta_{\mathrm{SC}})\cos(\phi_{\mathrm{SC}}) - \sin(\phi_{\mathrm{SC}})\sin(\theta_{\mathrm{SC}}))F_{\mathrm{Rad},Z'}. \quad (3)$$

A blank run is used to fit for $F_{\mathrm{Rad},Z'}$ using the spacecraft angles $\theta_{\mathrm{SC}}, \eta_{\mathrm{SC}}, \phi_{\mathrm{SC}}$, calculated using the star-tracker data. Since the entire blank run is a long (almost 4 h) SM dwell time, the longer stretch of usable data can be split into 20 segments instead of just 4. Ten pairs of neighboring segments can then be used in Eq. (1) to provide ten independent linear least squares fits for $F_{\mathrm{Rad},Z'}$, recalling that the source mass is static through the blank run and therefore $a^{(2)}_{\mathrm{Grav,SM}} - a^{(1)}_{\mathrm{Grav,SM}} = 0$.

Figure 4 shows the $F_{\mathrm{Rad},Z'}$ fit results through the blank run. The solid red line shows the weighted mean of the independent estimates $(-7.876 \pm 0.048) \times 10^{-8}$ N, with an associated error shaded red. The weighted mean error was calculated using a quadrature sum of the errors for the individual points, plus a standard deviation between the points to account for their residual scatter. The resulting value for $F_{\mathrm{Rad},Z'}$ is then an average SRP force in the Sun-Earth direction through the blank run solar sail.

The magnitude of $F_{\mathrm{Rad},x}$ (SRP component on the test mass) through the blank run grew from -6×10^{-10} N to 12×10^{-10} N as the spacecraft rotated. Comparing this to the signal term in Eq. (1), around parts in 10^{-11} N for a source mass displacement of 600 μm, it can be said that a great deal of uncertainty in this method comes from a signal buried in background SRP "noise." Minimizing this parasitic force, either by calibration or isolation, will greatly enhance the quality of the measurement. This will be addressed again later when comparing the present method with a fuel consumption estimate.

D. Fitting the signal

For each of the ten solar sails where the source mass is moved, the gravitational acceleration signal term is calculated as

$$T_{\mathrm{sig}} = a^{(2)}_{\mathrm{Grav,SM}} - a^{(1)}_{\mathrm{Grav,SM}} = 2\frac{Gm_{\mathrm{SM}}}{d^3}\Delta r \quad (4)$$

where m_{SM} is the mass of the SM, d is the separation between the TM and SM when both are centered in their housings, and Δr is the total distance traveled by the SM between the two dwell positions. A linear least squares fit was performed for the value of G that minimized $\delta a^{\mathrm{res}}_{\mathrm{TM}}$ for each of the runs. The 15 remaining values, after vetoing four with large transients and interchanged TM/SM masses, are shown in Fig. 5.

The individual errors propagated from the fitting stages do not cover the scatter between points. This is thought to arise primarily from assumptions made about variability in the SRP force. In principle it is capable of changing value not only gradually in time as the solar output changes, but also within a solar sail as the projected spacecraft geometry in the plane perpendicular to the incident force changes. This effective force is not calibrated for and therefore could lead to large uncertainties in the values obtained.

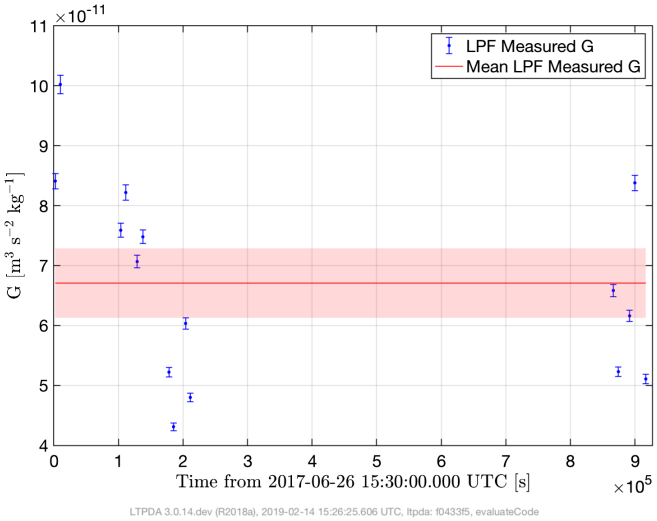

FIG. 5. Fit results for G as measured by LPF. The blue points show the independent measurements while the red solid line shows their weighted mean, with total error given by the red shaded area. The mean value found was $6.71 \pm 0.42(\times 10^{-11})$ m^3 s^{-2} kg^{-1}, a 6.3% relative error.

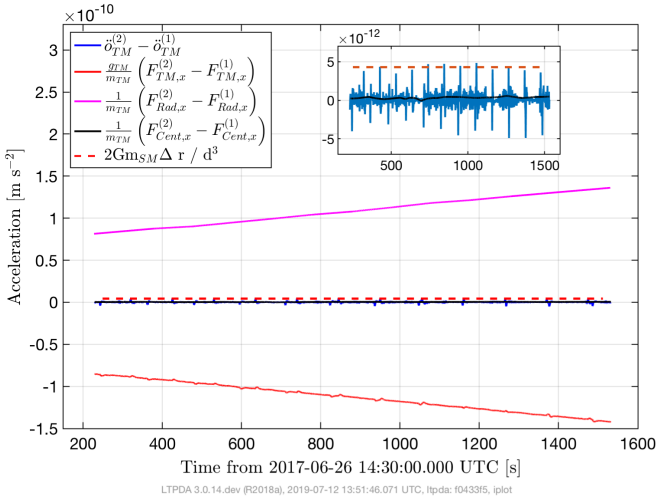

FIG. 6. Breakdown of the terms in Eq. (1) contributing to a single estimate of G, taken as a difference of the first two dwell times of the third solar sail, to demonstrate the order of magnitude of the signal term relative to the other noise terms. Inset: Zoom-in of central terms. Note the regular glitches in the differential acceleration channel and their amplitude relative to the signal term.

In principle the effect is pseudorandom. The spacecraft orientation from solar sail to solar sail is not deterministic as it depends on the initial alignment of the spacecraft, which varies from sail to sail, and so, in principle, the scatter can be averaged out using all 15 measurements. The mean value was then given a total error of the quadrature sum of individual errors, plus a standard deviation divided by the square root number of points to account for assumptions made in SRP variability. The final mean value was found to be $6.71 \pm 0.42(\times 10^{-11})$ m^3 s^{-2} kg^{-1}, a 6.3% relative error and in agreement with the CODATA 2014 recommended value of $6.67408 \pm 0.00031(\times 10^{-11})$ m^3 s^{-2} kg^{-1} to 1σ [7].

E. Analysis of errors

To further illustrate the role of the SRP force in this method, the first two dwell times of the third solar sail are subtracted one from the other and shown in Fig. 6. The pink line (top) is the component of the SRP force in the TM-SM axis, the red (bottom) is the electrostatic force on the TM in the TM-SM axis, the dashed red line (middle top) is the signal term using the value for G fit in this solar sail, and finally the blue (middle with glitches) and black (middle) show the differential acceleration between the two masses and the centrifugal force on the TM due to spacecraft rotation.

Note that the example of terms given here is from the beginning of a solar sail, where the component of the SRP force in the measurement axis is relatively small. As the spacecraft rotated through a solar sail, this term grew exponentially and further exaggerated the problem. Furthermore, given that the SRP force on the spacecraft was assumed constant both within and between solar sails, a small variability of this force can have an amplified effect on the signal due to the relative magnitudes. Unfortunately the blank run was only performed once, meaning analysis of the SRP variation *in situ* is limited to what is presented here and in [14].

Another difficulty encountered was the presence of glitches in SM dwell times with period 100s and amplitude comparable to the target signal. Notice in the inset of Fig. 6, showing a close-up of the central terms, regular glitches are clearly visible in the differential acceleration, $\ddot{o}_{\mathrm{TM}}$, and electrostatic force acting on the TM in the TM-SM direction, $F_{\mathrm{TM},x}$. Their amplitude is comparable to the signal term (dashed red) and although they are regular in time, their shape varies. Consequently, it was not possible to subtract a fit to their shape and their presence poses a systematic error.

In order to quantitatively assess if the SRP force and periodic glitches negatively affected the analysis, the number of G measurements can be increased by not limiting Eq. (1) to pairs of subsequent SM dwell times. In this situation, each positive SM displacement segment is subtracted from all negative SM displacement segments across all solar sails. This gives a total of 100 now dependent G estimates, shown in Fig. 7 as a function of the change in SM proximity to the TM, Δx_{SM}. The mean value using this extended population is $6.77 \pm 0.31(\times 10^{-11})$ m^3 s^{-2} kg^{-1}, a 4.6% $(\sigma/\sqrt{n})$ relative error. More importantly, there is a large variation between the points, particularly for the lower Δx_{SM} which spanned almost double the mean value extracted.

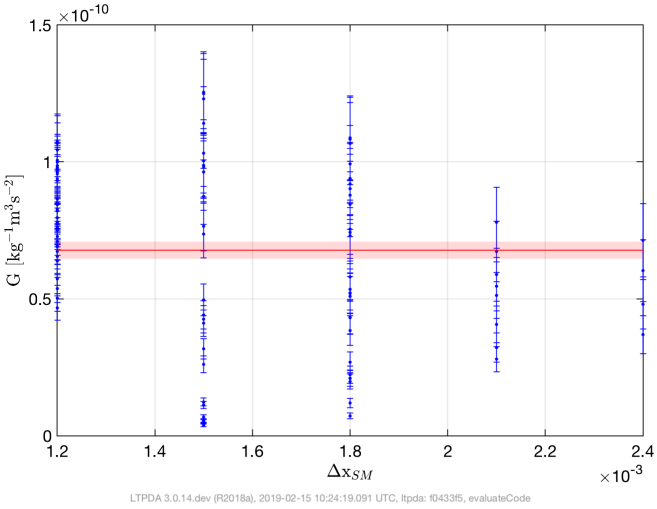

FIG. 7. Measurements of G using all 100 possible couplings between any pair of high resolution data segments. The mean value (red line, associated error shaded red) was found to be $6.77 \pm 0.31(\times 10^{-11})$ m^3 s^{-2} kg^{-1}, a 4.6% relative error.

TABLE I. Leading uncertainties in experiment 1 and their contribution to total relative error according to Eq. (6). δG_1 contains propagated uncertainties on averaging the independent measurements together, each of which is dominated by systematics such as glitches, while δG_2 corresponds to a standard $\sigma/\sqrt{n}$ error to account for implicit assumptions leading to a scatter between values.

Parameter	Value	Error	Units	$\delta\bar{G}/\bar{G}$
d	37.6	0.0052	cm	3.38×10^{-4}
m_{TM}	1.9282	0.0005	kg	6.88×10^{-5}
m_{SM}	1.928	0.0005	kg	6.88×10^{-5}
g_{TM}	1.0786	0.0095	N/A	2.34×10^{-3}
$F_{\mathrm{Rad},Z'}$	−7.876	0.048	$\times 10^{-8}$ N	1.63×10^{-3}
$\delta\bar{G}_1$	0.0193	N/A	$\times 10^{-11}$ kg^{-1} m^3 s^{-2}	N/A
$\delta\bar{G}_2$	0.423	N/A	$\times 10^{-11}$ kg^{-1}m^{3}s^{-2}	N/A
$\delta\bar{G}_{\mathrm{tot}}$	0.42	N/A	$\times 10^{-11}$ kg^{-1}m^{3}s^{-2}	N/A

The residuals of Eq. (1), $\delta a_{\mathrm{TM}}^{\mathrm{res}}$, can be used to qualitatively assess the variation not accounted for in the model. A mean residual of $-3.9 \pm 23.6(\times 10^{-12})$ ms^{-2} was found for the extended population of measurements, suggesting no significant direct current term has been excluded in the model used. The 1σ error is of the same order as the signal, $\pm 6 \times 10^{-12}$ ms^{-2}, emphasizing that the signal term was not loud enough to overcome the variability in the background terms not accounted for in the model. Furthermore, a 100% change in G, as shown in Fig. 7, corresponds to <1% variation in SRP force. This magnitude of variation in $F_{\mathrm{Rad},Z'}$ is not impossible over the time span of the experiment, and therefore could explain some of the scatter in Fig. 5.

The main contributions to the final error are outlined in Table I. The leading uncertainty on the ith independent G measurement is

$$\left(\frac{\delta G_i}{G_i}\right)^2 = 9\left(\frac{\delta d}{d}\right)^2 + \left(\frac{\delta m_{\mathrm{SM}}}{m_{\mathrm{SM}}}\right)^2 + \left(\frac{\delta g_{\mathrm{TM}}}{g_{\mathrm{TM}}}\right)^2 + \left(\frac{\delta F_{\mathrm{Rad},Z'}}{F_{\mathrm{Rad},Z'}}\right)^2 + \left(\frac{\delta m_{\mathrm{TM}}}{m_{\mathrm{TM}}}\right)^2 \quad (5)$$

where the contributions from the right-hand side of Eq. (1) are dominated by systematics; uncertainties from measurements such as spacecraft angles and interferometry readouts are comparatively negligible relative to absolute distances and masses. The final G value for experiment 1 is a mean average between $n = 15$ measurements $\bar{G} = \sum_{i=1}^{n} \frac{G_i}{n}$, with a propagated systematic error of $\delta\bar{G}_1 = \frac{1}{n}\sqrt{\sum_{i=1}^{n}(\delta G_i)^2}$, which corresponds to a relative uncertainty of

$$\frac{\delta\bar{G}_1^2}{\bar{G}^2} = \left(9\left(\frac{\delta d}{d}\right)^2 + \left(\frac{\delta m_{\mathrm{SM}}}{m_{\mathrm{SM}}}\right)^2 + \left(\frac{\delta g_{\mathrm{TM}}}{g_{\mathrm{TM}}}\right)^2 + \left(\frac{\delta F_{\mathrm{Rad},Z'}}{F_{\mathrm{Rad},Z'}}\right)^2 + \left(\frac{\delta m_{\mathrm{TM}}}{m_{\mathrm{TM}}}\right)^2\right)\sum_{i=1}^{n}\frac{1}{n^2}\frac{G_i^2}{\bar{G}^2}. \quad (6)$$

The second error, added to account for assumptions implicit in the model (e.g., constant $F_{\mathrm{Rad},Z'}$), is a standard deviation between the independent measurements divided by the root of the number of measurements; $\delta\bar{G}_2 = \sqrt{\frac{1}{n(n-1)}\sum_{i=1}^{n}(G_i - \bar{G})^2}$. The final measurement uncertainty is then the quadrature sum of the two errors $\Delta\bar{G}_{\mathrm{tot}} = \sqrt{\delta\bar{G}_1^2 + \delta\bar{G}_2^2}$, shown at the bottom of Table I.

The dominating systematic errors in δG_1 are the uncertainties in the DC values of the gain and SRP force. To improve the results of this experiment, it is important to calibrate these terms more accurately. This would include more blank runs to take into account the variability of the SRP force both between solar sails and within a solar sail. The change in the component of the SRP force in the measurement axis due to geometric effects as the space raft rotates was not taken into account. By including more blank runs, this effect could be better characterized. In addition, specific testing of the solar sail mode would identify ways to avoid glitches in the data and reduce their impact on the fits.

A more accurate calibration of both d and m_{SM} is necessary to improve δG_1. Since these parameters did not vary in time, their calibration was not as stringent preflight as other components of the LPF technology. Therefore calibrating them to a better precision would not pose a limiting factor in optimizing this experiment. However, it is also noted that their absolute values were specifically chosen, and altering them to boost the signal term could pose a threat to LPF's performance.

In order to reduce the random errors in δG_2, which dominated over δG_1 in the total error, a better understanding of the second order effects in the model is needed. Several of the signal runs were identical in conditions but exhibited very different values for G. Since all other factors were the same between these subsequent runs, it stands to reason that other disturbances in the spacecraft were not accounted for in the model. If this experiment is to be repeated, understanding the source of this variation is essential.

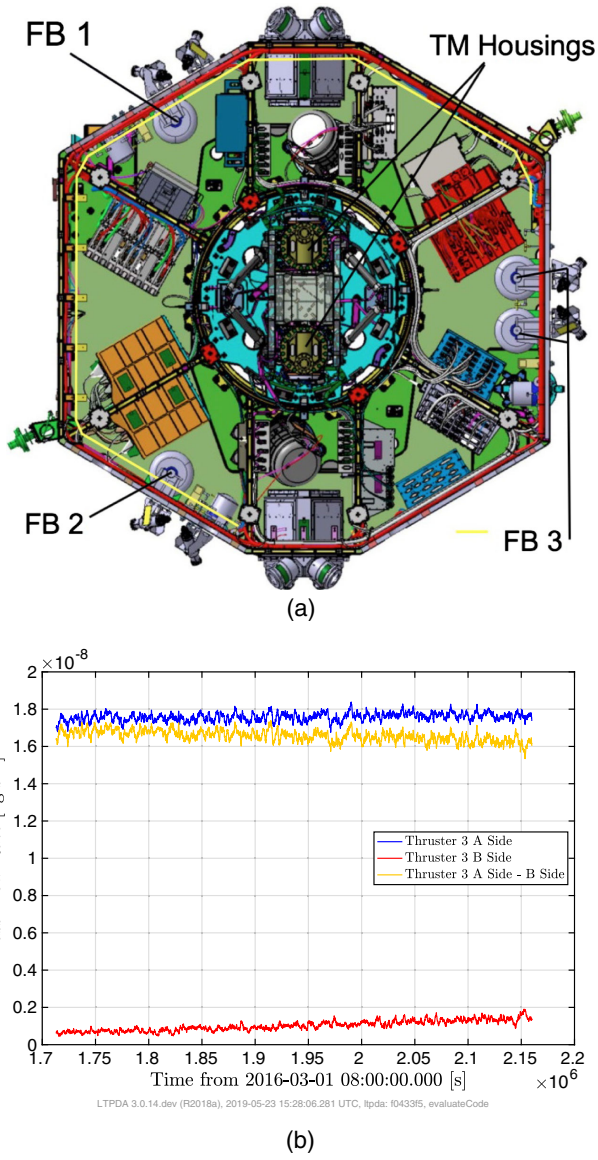

FIG. 8. (a) Diagram of spacecraft surrounding the central LISA Technology Package. Three fuel tank feed branches (FBs) are indicated. (b) Thruster 3 mass flow as measured by the sensors for both A (blue) and B (red) sides. Although the B side is off, there is a nonzero rate measured. Subtracting the B side from the A side (yellow) corrects for the DC offset and some of the drift.

III. EXPERIMENT 2

A. Method

The second experiment derived a signal from a variable SM outside of the main interferometry. The change in mass of the fuel tanks through the LPF nominal mission produced a time dependent correction to the main observable Δg_x. Three separate feeds from four tanks located in the spacecraft changed the mass distribution of the satellite uniquely. As the fuel was consumed, the magnitude of the fuel mass correction, $\Delta g_x^{\mathrm{fuel}}$, was proportional to big G.

Figure 8(a) shows the layout of the surrounding spacecraft material looking down through the solar array. Feed branches 1, 2 and 3 are labeled along with the two test mass housings. Feed branch i has a correction to $\Delta g_x^{\mathrm{obs}}$ characterized by $\Delta g^{\mathrm{fuel}} = \kappa_i G dm_i/dt$ with κ_i a constant geometric factor computed by finite element models, and dm_i/dt the mass flow rate of the ith tank. G is the gravitational constant, assumed to be 6.67×10^{-11} $\mathrm{m^3\,s^{-2}\,kg^{-1}}$ in nominal mission experiments [15].

By introducing a multiplicative factor A on $\Delta g_x^{\mathrm{fuel}}$, it is possible to use the fuel tanks as a makeshift source mass and fit for the value of G by scaling the assumed value. The model used here for $\Delta g_x^{\mathrm{obs}}$ is

$$\Delta g_x^{\mathrm{obs}} = A\Delta g_x^{\mathrm{fuel}} + \Delta g_x^{P} \tag{7}$$

where $\Delta g_x^P(t)$ is the relative differential acceleration between the two TMs due to pressure changes, proposed to be a combination of out-gassing effects and thermal fluctuations affecting residual gas pressure [15]. The model used here is

$$\Delta g_x^P(t) \approx P_0 \left(\frac{24 \times 60 \times 60}{t - T_0} \right)^{\alpha} + C_0 \tag{8}$$

where P_0 is an amplitude for the pressure induced relative acceleration, C_0 is a DC correction, and T_0 is a time from launch to ventilation, where the inside of the spacecraft began outgassing, set at 37 days. The index α describes the decay of the residual gas effects on the relative acceleration, and it is predicted to be a mix of two power laws. When $\alpha = 0.5$, the model describes temperature fluctuations affecting residual gas pressure in the housings, and when $\alpha = 1.0$, it describes ventilation of gas in the housings to the vacuum outside the spacecraft.

There was an option to include T_0 in the set of fit parameters $\{P_0, \alpha, C_0, A\}$. Doing so would allow a better mixing of the power laws mentioned previously, as it is not clear that setting T_0 to the ventilation date would allow the model to fully capture effects due to both temperature fluctuations and with outgassing. However, in this analysis it was noted that the knowledge of the fuel tank geometries and proximity to the test masses limit the extent to which a full fit could be performed on the data. Furthermore, second order effects such as thermal behavior within each $\Delta g_x^{\mathrm{obs}}$ segment were not included, limiting the scope of the analysis. For these reasons it was decided that for a proof of concept it is not necessary to allow T_0 to vary in the fits, but it is noted as an essential improvement.

The LPF cold gas propulsion system comprises three tanks, or feed branches, of gaseous nitrogen which is slowly released through valves to provide μN thrusts to the spacecraft. For each tank, there are two primary nozzles (A side) and two redundant nozzles (B side), with the B side closed while the A side is open and vice versa. Each nozzle

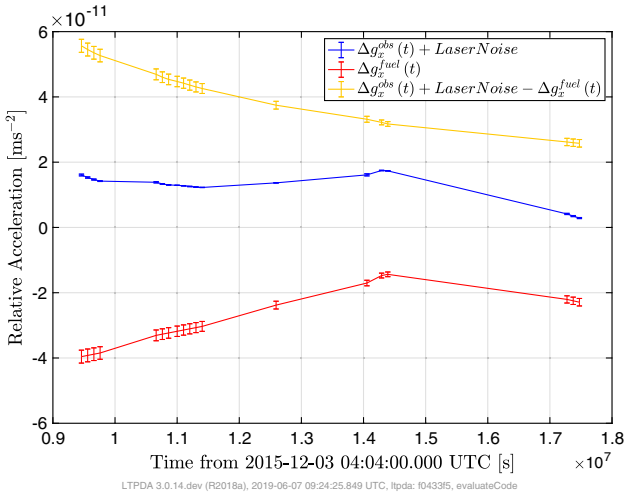

FIG. 9. Data used for experiment 2 fits. The $\Delta g_x^{\mathrm{obs}}$ (blue, with laser noise) are corrected for a variable fuel tank mass $\Delta g_x^{\mathrm{fuel}}$ (red) and a slow release of residual pressure in the TM housings Δg_x^{P} (yellow).

contains a mass flow sensor that feeds into a closed feedback loop with the relative acceleration between the two test masses. The zero-points (zero mass flow) of the nozzles are therefore not constrained as well as the scientific equipment, especially in DC flow. Consequently, there is a nonzero and drifting zero-point mass flow registered by the sensors. Figure 8(b) shows the measured mass flow through an example nozzle for both the A (blue, switched on) and B (red, switched off) sides. Note the drift and nonzero mass flow for the B side.

In order to compensate for this systematic error, the constant component of the zero-point offset are assumed the same for both the A and B sides. Hence, subtracting the B side from the A side [yellow data in Fig. 8(b)] should only leave the drifting component, which can then be characterized by a peak-to-peak error when taking the mean. In practice this corresponds to around 5% relative error for the total mass flow from a tank.

For the segments of $\Delta g_x^{\mathrm{obs}}$, 11 measurements were taken across the nominal mission, all using the lowest possible force and torque authorities in the mission (50 pN and 1.5 pNm on TM2, 0 pN and 1 pNm on TM1 [13]). This ensured that no systematic errors were encountered by different levels of cross talk in each measurement run. Furthermore, the low suspension forces allowed for quieter runs and therefore better measurements relative to other $\Delta g_x^{\mathrm{obs}}$ configurations. Each run typically lasted 1–2 days and was averaged to a mean with standard deviation error in order to average out noise in the data. Figure 9 shows the data used for the fit. The observed $\Delta g_x^{\mathrm{obs}}$ are shown in blue, $\Delta g_x^{\mathrm{fuel}}$ in red and the resulting pressure outgassing law in yellow for the simple example $A = 1$.

The log-likelihood was taken as a Gaussian, with width dependent on choice of A since this parameter scales the

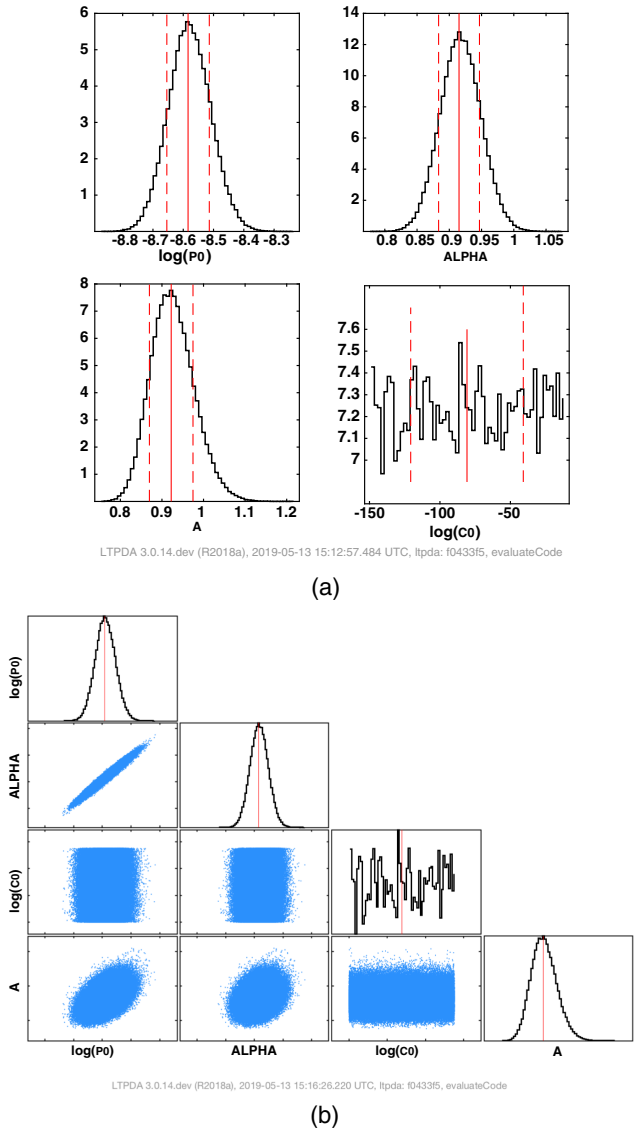

FIG. 10. (a) Posterior distributions for a simplified model to describe the trend of DC Δg_x measurements through the LPF nominal mission. All marginalized distributions were Gaussian except $\log_{10}(C_0)$, which was not constrained by the fit. Repeating the fits excluding C_0 produced the same posterior distributions. (b) Posterior correlations for a simplified model to describe the trend of DC Δg_x measurements through the LPF nominal mission. The large error bars on the fuel consumption data meant the fit was not sensitive anymore to changes in C_0. A strong correlation is observed between α and $\log_{10}(P_0)$, while weak correlations are observed in the remaining parameters.

$\Delta g_x^{\mathrm{fuel}}$ data and their associated errors. The algorithm is therefore biased to lower values of A, which reduce the overall errors in the fit. The log-likelihood used for the fit is

$$\log \mathcal{L} = -\sum_i \log\left(\sqrt{2\pi\sigma_i^2}\right) - 0.5\sum_i \frac{(\Delta g_x^{\mathrm{obs}} - y_i)^2}{\sigma_i^2} \qquad (9)$$

for $y_i = A\Delta g_{x,i}^{\mathrm{fuel}} + \Delta g_{x,i}^{P}$ and variance $\sigma_i^2 = (\delta\Delta g_{x,i}^{\mathrm{obs}})^2 + A^2(\delta\Delta g_{x,i}^{\mathrm{fuel}})^2$ for each of the i points created by averaging

TABLE II. Leading uncertainties for experiment 2. $\delta\Delta g_x^{\mathrm{fuel}}$ includes the systematic uncertainties associated with geometric knowledge of the experiment (in finite element model calculations of κ_i) and measurement errors from the mass flow sensors (in $\dot{m}_i$). The final relative error on G is then the relative error extracted for A in the fits, which is dominated by $\dot{m}_i$ in $\delta\Delta g_x^{\mathrm{fuel}}$.

Parameter	Value	Error	Rel. error (%)	Units
κ_i	ARRAY	ARRAY	0.8	m^{-2}
$\dot{m}_i$	ARRAY	ARRAY	$\lesssim$4.5	$\mathrm{kg\,s}^{-1}$
$\delta\Delta g_x^{\mathrm{fuel}}$	ARRAY	ARRAY	$\lesssim$4.6%	$\mathrm{kg}^{-1}\,\mathrm{m}^3\,\mathrm{s}^{-2}$
$\delta\Delta g_x^{\mathrm{obs}}$	ARRAY	ARRAY	$\lesssim$1.7%	$\mathrm{kg}^{-1}\,\mathrm{m}^3\,\mathrm{s}^{-2}$
$\log_{10}(P_0)$	−8.584	0.070	0.82	$\log_{10}(\mathrm{ms}^{-2})$
α	0.915	0.032	3.5	N/A
$\log_{10}(C_0)$	−81	40	50	$\log_{10}(\mathrm{ms}^{-2})$
A	0.922	0.052	5.6	N/A
G	6.15	0.35	5.6	$\times 10^{-11}\mathrm{kg}^{-1}\mathrm{m}^3\mathrm{s}^{-2}$

over 10^5 s of $\Delta g_x^{\mathrm{obs}}(t)$ data. This was done to average out temperature fluctuations within each Δg_x run as only long term trends between runs are relevant for the fits and temperature was assumed constant from run to run in the nominal mission. All prior distributions were taken as uniform and over wide ranges to allow the algorithm to fully explore possible correlations. Large errors in the data also meant using informative priors would risk overbiasing the fit.

B. Fit results

A Markov chain Monte Carlo algorithm was run for 4 million draws and exhibited convergence on the posterior values. Figures 10(a) and 10(b) show the results, where correlations are observed between all parameters except C_0.

The marginalized posteriors for P_0, α and A are Gaussian with correlations seen among all three parameters, shown in the corner plot of Fig. 10(b). The posterior for C_0 is unbounded from below, indicating the data uncertainties were too large for the fit to be sensitive to this parameter.

Table II summarizes the main contributions to the uncertainties of each point and the posterior values from the fit. The uncertainties in each point are dominated by the measurement errors in the $\dot{m}_i$ values used, and the systematic uncertainties in the geometric knowledge of the experiment, included in κ_i. The 1σ errors of each parameter are also shown, with a large variation in relative magnitude. The most constrained fit parameter was α, with a relative error of 3.5%, while the least constrained was C_0, which was not constrained by the fit. Repeating these fits excluding C_0 yielded the same posterior values and 1σ errors for the remaining parameters. The fit result for A shows that the fuel correction through the nominal mission was significant enough to provide a signal for A matching the dedicated experiment results despite using a change in mass of only a few hundred grams at a comparable distance of around 1 m.

Figure 11 shows the best fit model (red), calculated using the posterior values and errors in Table II, with the observed $\Delta g_x^{\mathrm{obs}}$ data (blue). Shaded areas indicate the error in the data or model and underline that the uncertainty in the model was dominated by the uncertainties in the mass flow sensor data. Had this been calibrated outside the control loop, the fit parameter posteriors could have been more narrow and the best fit model error region a tighter match to the observed data.

The value for α obtained was very close to a perfect outgassing power law of 1. This suggests that the thermal fluctuations had a negligible effect on the residual gas pressure within the housings, which could be a result of using many $\Delta g_x^{\mathrm{obs}}$ data through the entire nominal mission. Doing the analysis in this way allowed for averaging over thermal fluctuations in each data segment, thereby averaging out this effect and biasing to an almost perfect outgassing law.

The value of A found corresponds to $G = 6.15 \pm 0.35(\times 10^{-11})$ $\mathrm{m}^3\,\mathrm{kg}^{-1}\,\mathrm{s}^{-2}$, a 1σ relative error of 5.6%, and again in agreement with the 2014 recommended value of $6.67408 \pm 0.00031(\times 10^{-11})$ $\mathrm{m}^3\,\mathrm{s}^{-2}\,\mathrm{kg}^{-1}$ to 2σ [7]. The relative ease of this method coupled with the better end error on the value obtained underlines the importance of

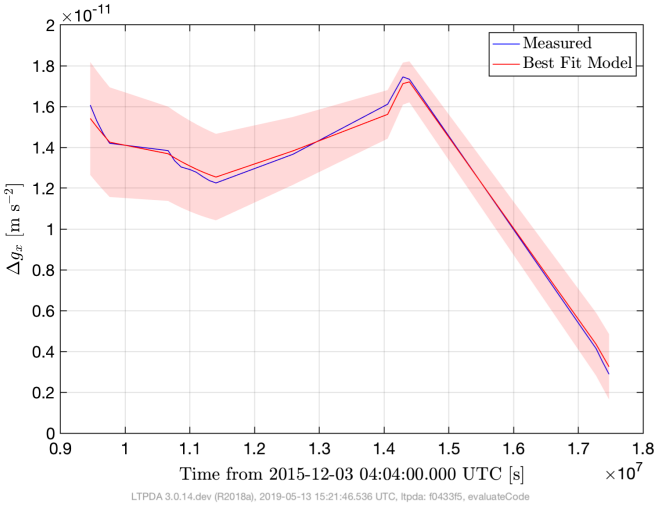

FIG. 11. Posterior model with data. Large errors on the mass flow data allowed a larger spread in possible fit parameters.

using the drag-free control when using interferometers to measure big G.

C. Analysis of errors

The results of this method show that a relatively easy measurement of the gravitational constant can be made with a source mass and interferometer. Looking at Table II, the leading contributions to the posterior error on A were in the fuel tank positions, dimensions and mass flow rates, which were not calibrated to the same precision as other components of the LISA LPF experiment.

Systematic uncertainties in geometry were contained in the finite element calculations of κ_i, which to first order behaved as $1/R^2_{\mathrm{SM-TM}}$ where $R_{\mathrm{SM-TM}}$ is the absolute distance between the fuel tank and the closest TM. Measurement errors in $\dot{m}_i$, due to a zero-point flow that was difficult to extract and correct for, dominated the statistical uncertainty in the fit. The majority of the LPF analyses were done in frequency domain, which placed less stringent requirements on absolute values used to calculate and measure these parameters; therefore by more accurately measuring geometric properties preflight, and using out of loop mass flow sensors, the leading contributions to the uncertainty can be drastically improved. The end uncertainty on A is then given by next order terms in the model.

Two improvements to the model can be identified from this analysis. First, the exact time to venting, T_0, can also be fit to correctly allow for a more flexible mixing of the pressure models. Second, thermal fluctuations within each $\delta g_x^{\mathrm{obs}}$ segment can be included, instead of averaging over 10^5 s segments of data. This could be done by fitting a thermal coefficient to transform changes in temperature to a thermal correction δg_x^{th}.

A different approach for this method would be to measure a constant outflow of material over a period of several days to decrease the influence of the pressure variation Δg_x^P. However, it is noted that this approach would require a good understanding of the thermal transfer function on the DC $\Delta g_x^{\mathrm{obs}}$ data. Another approach would be a larger SM closer to the TMs to increase the signal to noise ratio. Since the SMs are independent of the central interferometry system, it is possible to use many SMs with varying total masses and at a variety of locations without risking the LPF performance.

When optimizing the method, it is relatively easier to have a gaseous source mass quickly released than to move a solid source mass closer to the interferometric system. Doing so would require a second optical bench to track the source mass position as it is moved. Using instead several calibrated gas tanks at various locations would maximize the signal by changing the signs of the κ_i without the need to simultaneously track positions.

IV. DISCUSSION

Experiment 1 exhibited several difficulties, such as periodic glitches and a coupling of the SRP force into the measurement axis. Redesigning the experiment to mitigate these effects would require many more injection and blank runs to properly characterize the variability of these effects. Conversely, the limiting factor in experiment 2 was the measurement of the mass flow rates. Having mass flow sensors outside of the closed control loops would allow a much more precise measurement of this parameter and already improve the results.

The relative amount of work to extract the signal in experiment 1 was greater than in experiment 2. The latter required only one fit rather than three consecutive fits in the former. With several dependent fits, it was difficult to disentangle the effects of errors in the final result, for example how the glitches are fed through the analysis.

Experiment 2 also demonstrated that a mass change of a few hundred grams around a meter away is enough to induce a measurable signal, whereas a mass movement of hundreds of microns half a meter away was almost lost in the background of experiment 1. This emphasizes the need to use drag-free control to decouple the background forces from the measurement.

Experiment 2 also has greater flexibility for optimization compared to experiment 1. One possibility is shorter term measurements of days rather than months to decrease the effects of pressure changes. Using several SM tanks located near each TM, and staggering the release of material, the sign for each κ_i is reversed and the signal to noise ratio maximized. Quick releases of large volumes of gas between consecutive noise measurements would decrease the relative error of the mass flow; measuring the total gas emitted rather than trying to accurately measure a slow stream of material is relatively easier to do. In contrast, experiment 1 requires costly repetitions of blank and injection runs which are limited in returns. Ultimately, a redesign to increase the SM mass and minimize the SM-TM distance is necessary to boost the signal; however this is detrimental to the performance of the interferometer in which masses and distances were specifically chosen.

Comparing the results, it is clearly beneficial to use drag-free control when designing an experiment to measure big G. This allows the experiment to be shielded from the external background forces that would otherwise drown the signal. Furthermore, the performance of a drag-free interferometer in space has already been demonstrated. Additional source masses can then be placed on the spacecraft to maximize signal to noise, with little risk to the performance. Finally, after optimizing the layout of SMs and the release of material, systematic uncertainties in the geometric properties of the experiment need to be accurately calibrated to reach a competitive measurement of at least parts in 10^4.

V. CONCLUSION

Both the dedicated experiment and the fuel consumption estimate yielded values of big G that are consistent with each other, and with the literature values from ground

estimates. The end errors were both around 5%–10%, but with drastically different compositions; together they pinpoint the complexities to be addressed in designing a space based experiment to measure big G.

The use of drag-free control interferometry was shown to be a much more powerful tool to isolate the experiment from sources of noise that would otherwise drown out the signal. The success of the LPF mission was a large factor in the success of experiment 2, and it is noted that the LPF DC noise budget reached was not limiting in the results of this method. Therefore, should the choice be made, resources can be allocated to optimizing the gaseous source masses for a stronger signal instead of the noise budget of the system.

Competitive measurements of big G in space would provide experimental fundamental physics with a way to challenge the disparity in the terrestrial measurements observed to date. As has been noted by the gravitational community, moving to space affords a much more quiet environment [16–18], isolating many of the noise sources that could be the source of disagreements in recent measurements. It is hoped that the findings outlined here will facilitate this endeavor and help pave the way for even more precise measurements of this elusive universal constant.

ACKNOWLEDGMENTS

This work has been made possible by the LISA LPF mission, which is part of the space-science program of the European Space Agency. The French contribution has been supported by the CNES (Accord Specifique de projet CNES 1316634/CNRS 103747), the CNRS, the Observatoire de Paris and the University Paris-Diderot. E. P. and H. I. would also like to acknowledge the financial support of the UnivEarthS Labex program at Sorbonne Paris Cité (ANR-10-LABX-0023 and ANR-11-IDEX-0005-02). The Albert-Einstein-Institut acknowledges the support of the German Space Agency, DLR. The work is supported by the Federal Ministry for Economic Affairs and Energy based on a resolution of the German Bundestag (FKZ 50OQ0501 and FKZ 50OQ1601). The Italian contribution has been supported by Agenzia Spaziale Italiana and Istituto Nazionale di Fisica Nucleare. The Spanish contribution has been supported by Contracts No. AYA2010-15709 (MICINN), No. ESP2013-47637-P, No. ESP2015-67234-P, No. ESP2017-90084-P (MINECO), and No. 2017-SGR-1469 (AGAUR). M. N. acknowledges support from Fundación General CSIC (Programa ComFuturo). F. R. acknowledges support from a Formación de Personal Investigador (MINECO) contract. The Swiss contribution acknowledges the support of the Swiss Space Office (SSO) via the PRODEX Programme of ESA. L. Ferraioli is supported by the Swiss National Science Foundation. The UK groups wish to acknowledge support from the United Kingdom Space Agency (UKSA), the University of Glasgow, the University of Birmingham, Imperial College, and the Scottish Universities Physics Alliance (SUPA). J. I. T. and J. S. acknowledge the support of the U.S. National Aeronautics and Space Administration (NASA).

[1] R. Newman, M. Bantel, E. Berg, and W. Cross, A measurement of G with a cryogenic torsion pendulum, Phil. Trans. R. Soc. A **372**, 20140025 (2014).
[2] H. Parks and J. Faller, Simple Pendulum Determination of the Gravitational Constant, Phys. Rev. Lett. **105**, 110801 (2010).
[3] M. Prevedelli, L. Cacciapuoti, G. Rosi, F. Sorrentino, and G. M. Tino, Measuring the Newtonian constant of gravitation G with an atomic interferometer, Phil. Trans. R. Soc. A **372**, 20140030 (2014), p. 1.
[4] G. Rosi, F. Sorrentino, L. Cacciapuoti, M. Prevedelli, and G. M. Tino, Precision measurement of the Newtonian gravitational constant using cold atoms, Nature (London) **510**, 518 (2014).
[5] S. Schlamminger, E. Holzschuh, W. Kündig, F. Nolting, R. E. Pixley, J. Schurr, and U. Straumann, Measurement of Newton's gravitational constant, Phys. Rev. D **74**, 082001 (2006).
[6] T. Quinn, C. Speake, H. Parks, and R. Davis, The BIPM measurements of the Newtonian constant of gravitation, G, Phil. Trans. R. Soc. A **372**, 1 (2014).
[7] P. J. Mohr, D. B. Newell, and B. N. Taylor, CODATA recommended values of the fundamental physical constants: 2014, Rev. Mod. Phys. **88**, 035009 (2016).
[8] J. D. Anderson, G. Schubert, V. Trimble, and M. R. Feldman, Measurements of Newton's gravitational constant and the length of day, Europhys. Lett. **110**, 10002 (2015).
[9] M. Pitkin, Comment on "Measurements of Newton's gravitational constant and the length of day" by Anderson J. D. et al., Europhys. Lett. **111**, 30002 (2015).
[10] M. Armano *et al.*, Sub-Femto-g Free Fall for Space-Based Gravitational Wave Observatories: LISA Pathfinder Results, Phys. Rev. Lett. **116**, 231101 (2016).
[11] M. Armano *et al.*, Beyond the Required LISA Free-Fall Performance: New LISA Pathfinder Results down to 20 μHz, Phys. Rev. Lett. **120**, 061101 (2018).
[12] C. Trenkel, LPF G outline (private communication).
[13] M. Armano *et al.*, Calibrating the system dynamics of LISA Pathfinder, Phys. Rev. D **97**, 122002 (2018).
[14] J. Baird, Experiments with LISA Pathfinder: Cosmic rays and fundamental physics, Chap. 4, Ph.D. thesis, Imperial College London, 2018, http://hdl.handle.net/10044/1/59662.

[15] M. Armano *et al.*, Temperature-induced forces on geodesic reference masses for LISA: Results from LISA Pathfinder (to be published).

[16] E. Hardy *et al.*, Testing the equivalence principle in space: The MICROSCOPE mission, in *42nd COSPAR Scientific Assembly* (2018), Vol. 42, p. H0.1-1-18.

[17] P. Touboul *et al.*, MICROSCOPE Mission: First Results of a Space Test of the Equivalence Principle, Phys. Rev. Lett. **119**, 231101 (2017).

[18] J. Berge, ISLAND: The inverse square law and Newtonian dynamics space explorer, in *42nd COSPAR Scientific Assembly* (2018), Vol. 42, p. H0.3-6-18.